AIAA
TP
89-0045

# AIAA'89

A89-25039

AIAA-89-0045

# CFD Simulation of Square Cross-Section, Contoured Nozzle Flows: Comparison With Data

Mark J. Ostrander, Aerojet Techsystems Co.,
Sacramento, California

Scott R. Thomas, Randall T. Voland, Robert W. Guy,
NASA Langley Research Center,
Hampton, Virginia

Shivakumar Srinivasan,
Analytical Services and Materials, Inc.,
Hampton, Virginia

RECEIVED
1989 JAN 13 P 1:07
ANALYTICAL SERVICES

**27th Aerospace Sciences Meeting**
January 9-12, 1989/Reno, Nevada

For permission to copy or republish, contact the American Institute of Aeronautics and Astronautics
370 L'Enfant Promenade, S.W., Washington, D.C. 20024

# CFD SIMULATION OF SQUARE CROSS-SECTION, CONTOURED NOZZLE FLOWS: COMPARISON WITH DATA

Mark J. Ostrander*
Aerojet Techsystems Company
Sacramento, California

A89-25039

Scott R. Thomas,† Randall T. Voland,†† Robert W. Guy††
NASA Langley Research Center, Hampton, Virginia

Shivakumar Srinivasan*
Analytical Services & Materials, Inc., Hampton, Virginia

## Abstract

Computational analyses have been made of the flow in NASA Langley's Arc-Heated Scramjet Test Facility's Mach 4.7 and Mach 6 square cross-section contoured nozzles for comparison with experimental results. The analyses, which were performed using a 3-D RANS computer code assuming a single species gas with constant specific heats, were intended to provide insight into the nature of the flow development in this type of nozzle. The computational results showed the exit flow distribution to be affected by counter-rotating vortices along the centerline of each nozzle sidewall. Calculated flow properties show general,but not complete, agreement with experimental measurements in both nozzles.

## Nomenclature

| | |
|---|---|
| $A_{exit}$ | nozzle exit area |
| $A_{IN}$ | area of inflow boundary for CFD calculation |
| $A_{throat}$ | nozzle throat area |
| $C_p$ | specific heat at constant pressure |
| $C_v$ | specific heat at constant volume |
| $M_1$ | Mach number |
| $M_{IN}$ | Mach number of flow at inflow boundary for CFD calculation |
| MW | molecular weight |
| $P_1$ | static pressure |
| $P_{t,1}$ | total pressure (in facility plenum chamber) |
| $T_1$ | static temperature |
| $T_{t,1}$ | total temperature (in facility plenum chamber) |
| $U_1$ | axial flow velocity |
| X | axial coordinate along nozzle length (zero at nozzle throat) |
| $X_{Ex1}$ | axial position of outflow boundary of computational region 1 |
| $X_{Ex2}$ | axial position of outflow boundary of computational region 2 |
| $X_{Ex3}$ | axial position of outflow boundary of computational region 3 |
| $X_{Ex4}$ | axial position of outflow boundary of computational region 4 |
| $X_{IN1}$ | axial position of inflow boundary of computational region 1 |
| $X_{IN2}$ | axial position of inflow boundary of computational region 2 |
| $X_{IN3}$ | axial position of inflow boundary of computational region 3 |
| $X_{IN4}$ | axial position of inflow boundary of computational region 4 |
| Y | vertical cordinate at each axial location (zero along nozzle centerline) |
| Z | horizontal coordinate at each axial location (zero along nozzle centerline) |
| $\rho_1$ | static density |
| $\rho_1 U_1$ | mass flow rate per unit area |

## Introduction

The NASA Langley Arc-Heated Scramjet Test Facility (AHSTF), has been used for testing scramjet engines and engine components for the past 12 years. This facility (Fig. 1) provides a test flow with total enthalpy, total pressure, and Mach number corresponding to actual flight conditions. An electric arc heats the air to a total temperature of approximately 8000° R. Unheated air is injected downstream of the arc heater to mix with this hot arc-heated air to produce the desired test conditions. By using two different square cross-section contoured nozzles with nominal exit Mach numbers of 4.7 and 6, flight conditions ranging from Mach 4.7 to Mach 8 can be simulated. Figure 2 shows schematics of these two facility nozzles. A calibration study of the flow exiting these nozzles was performed and the results were presented in Reference 1.

The present numerical study was conducted using an existing CFD code to provide insight into the development of the flow through these square cross-sectioned contoured nozzles. If the experimental results could be accurately reproduced numerically, the code could then be used with confidence for predictions of the nozzle flowfield at other tunnel conditions and in other facilities. These computational solutions also provide a much more complete description of the resultant flow than that which could be derived from the experimental results. Computed data can be obtained on a much finer grid, and local horizontal and vertical velocity components can be determined in addition to the axial velocity component. This more detailed data base is useful as inflow conditions for CFD analyses of the flow through test models such as scramjet engines.

## Computer Model

The computer program used in this analysis, developed by Ajay Kumar at NASA Langley, is described in Refs. 2 and 3. This program solves the three-dimensional Euler or Reynolds-averaged

*Aerospace Engineer, Member AIAA

†Aerospace Engineer, Hypersonic Propulsion Branch, High-Speed Aerodynamics Division

††Aerospace Engineer, Hypersonic Propulsion Branch, High-Speed Aerodynamics Division, Member AIAA



This paper is declared a work of the U.S. Government and is not subject to copyright protection in the United States.

Navier-Stokes equations in full conservation form by the explicit predictor-corrector method of MacCormack (Ref. 4). A two-layer algebraic eddy viscosity model is used to model turbulence (Ref. 5), and Sutherland's law is used for the calculation of molecular viscosity.

## Geometry

The nozzles analyzed in this study were square in cross section at all axial locations. Hence, only one quadrant of the nozzle flow was calculated since, by symmetry, this defined the entire flow. The solution for each nozzle was obtained by dividing an entire nozzle geometry into three or four axial regions (see Fig. 3). A solution was obtained for one region, and the exit flow from this region was used on the inflow boundary for the calculation of the next region. Setting the problem up in this way allowed larger time steps to be used in subsequent regions of the calculation since the time step limiting each computation was located at the inflow boundary near the wall. Therefore, the solutions were obtained in less computational time than would have been required to solve the entire nozzle geometry with the time step dictated by the flow near the nozzle throat. Also, by splitting the computation into regions, greater accuracy was achieved without generating prohibitively large file sizes. Figure 3 lists the axial length and inflow and outflow dimensions of each region, the grid size for each region, and the inflow Mach number for each test case.

Generating a physical grid for these square cross-section geometries was relatively easy. The grid for the entire nozzle was specified by a one dimensional array of X coordinates and a two-dimensional array of Y coordinates at each X station. The Z coordinates were obtained by reflecting the Y coordinates. A superposition of two exponential stretches produced a grid that was clustered near the wall and to a lesser extent near the symmetry plane in the transverse direction. This clustering near the symmetry boundaries was necessary to obtain a solution that was symmetric about the center-to-corner diagonal.

A comparison of the geometries of the square cross-section nozzles that were analyzed is shown in Fig. 4. This figure presents the wall contours normalized by the corresponding nozzle exit half-height versus the axial position normalized by overall nozzle length. These nozzles transition from a circular plenum to a square cross-section at the throat; however, none of the non-square upstream geometry was used in the calculations. Both have exit dimensions of approximately 11 x 11 inches.

## Boundary Conditions

For each nozzle calculation, the inflow conditions to the first axial nozzle region were specified as a uniform flow either just downstream of the throat (slightly supersonic flow) or upstream of the throat with subsonic flow. The flow variables at these inflow boundaries were held constant across the flow area except at the nozzle wall where no-slip and either adiabatic wall or isothermal (cold) wall conditions were used. Derivative conditions were used at the symmetry plane boundaries.

## Convergence

For each case, the code was run for a specified number of time steps to obtain a preliminary solution. After this solution was checked, the calculation was restarted and continued until the axial distribution of total calculated (integrated) mass flow varied less than 0.2% along the length of the nozzle; then, convergence to steady state was assumed. This convergence criterion was observed to be consistent with that described in Reference 2, since the calculations continued in time approximately equal to that required for the flow to traverse the flow domain three times.

# Results and Discussion

The initial effort undertaken in this study was to computationally model the nozzle flow conditions explored in Reference 1 and to compare the calculated nozzle exit flow parameters to those determined experimentally. The AHSTF test gas is arc-heated air; however, the CFD analysis was conducted assuming perfect gas. The average gas properties and the facility (test flow) stagnation conditions used in the nozzle computations are outlined in Table 1.

The experimental nozzle exit flow parameters (Mach number, mass flow rate per unit area, and static pressure) are presented in Fig. 5 for the AHSTF Mach 6 nozzle and in Fig. 6 for the AHSTF Mach 4.7 nozzle. Note the rather severe gradients along the centerline of each sidewall of the Mach 6 nozzle. Flow gradients in the Mach 4.7 nozzle were much less severe. As mentioned previously, the need for a better understanding of these experimental results prompted the CFD study of these nozzles.

## AHSTF Mach 6 Nozzle

The first computed test case involved simulation of the AHSTF Mach 6 nozzle using a 118 x 50 x 50 grid (over 4 regions); laminar flow was assumed with a supersonic inflow condition and an adiabatic wall boundary condition. Mach number contours at the nozzle exit from these calculations (Fig. 7) exhibited the general shape of the corresponding experimental contours shown in Fig. 5a. However, in the computed case, higher flow gradients were observed along the centerline of the nozzle wall than the experimental results.

The second computed test case repeated the conditions of the first test case with the exception that a finer grid of 178 x 75 x 75 points (again over 4 regions) was used. The Mach number contours resulting from this computation are shown in Fig. 8. Only slight differences were observed in comparison to Fig. 7, indicating that the grid size was small enough for sufficient resolution.

The third computed test case was also for the AHSTF Mach 6 nozzle with the finer grid and a supersonic inflow condition; however, for this case, the turbulence model was activated. Figs. 9a,b,c show the results of this computation with

an adiabatic wall assumption and Figs. 10a,b,c show the results with an isothermal wall (1000°R) assumption which should more closely represent the experimental case. Inclusion of the turbulence model yielded flow contours which compared much closer to the experimental results (Fig. 5) for the AHSTF Mach 6 nozzle. The computational results however, showed substantially more flow defects near the centerline of the wall and little difference was noted in the CFD results when the isothermal (cold) wall boundary condition was used instead of the adiabatic wall condition. This is further demonstrated in Fig. 11 by comparison of the centerline profiles of various parameters from both the experimental and computational results. In general, the CFD and experimental results compare very well near the center of the nozzle at locations more than approximately two inches away from the wall. The deficits in the flow properties within two inches of the wall are significantly higher in the computational solution than in the experimental results. This discrepancy may be due to inaccuracies in the CFD results because of the perfect gas assumptions, the viscosity model, and the flow turbulence model in predicting gas properties at these high temperatures. Conversely, the experimental data may be in error near the wall on the centerline because of the effect of flow angularity on the probe measurements.

The agreement between the experimental data and the numerical solution in the bulk of the flow (i.e. in the center portion) indicates that the CFD code is resolving the general characteristics of the test flow through the nozzle expansion process in this area. However, the disagreement near the wall on the centerline yields uncertainty of the flow resolution in this area. The CFD results will nevertheless be used to show the probable nature of the flow development throughout the nozzle expansion. The velocity vectors (in one quadrant) of the flow in the vertical/horizontal (Y-Z) plane are presented in Fig. 12 for four approximately equally-spaced axial intervals along the nozzle length (for the calculation with adiabatic wall assumptions). The corresponding static pressure contours (also in one quadrant) are shown in Fig. 13 for the same intervals. In the initial expansion (shown in Figs. 12a and 13a by the velocity vectors and static pressure contours at an axial station of x = 14.93 inches), the flow vectors in the transverse plane are directed away from the center of the nozzle with the preponderant direction towards the nozzle corner. The maximum velocity in this plane is approximately 10% of the axial velocity component. (Note that transverse velocity vectors would also exist in the y-direction early in the expansion if the nozzle were only contoured on two surfaces perpendicular to the y-direction.) The pressure becomes increasingly higher near the corner of the nozzle. As indicated by the decrease in magnitude of the transverse velocity vectors at the exit of the second axial region (x = 30.12, Fig. 12b and 13b); the higher pressure in the corners of the nozzle has slowed the flow in the boundary layer and caused a flow deflection such that the flow near the wall is turned away from the corner. The transverse velocity vectors near the center of the nozzle are much smaller than those near the corners and in the boundary layer and there is an inflow to the center. The pressure near the corners is still greater than that near the centerline of the nozzle (Fig. 13b). The flow solution at the exit of the third axial region (x = 45.1 inches) shows that the transverse boundary layer flow has been diverted from adjacent nozzle corners, has met along the nozzle wall centerline, and has been diverted parallel to and then away from the nozzle center plane. This shows the beginning of the formation of counter-rotating vortices which are shed during the nozzle expansion and are a characteristic of the nozzle exit flow. Also, note that in the exit of the third axial nozzle region, the static pressure distribution is much different in that the pressure is now highest near the center of the nozzle and has dropped significantly near the corners. This indicates that shock wave systems were generated in the expansion process since the nozzle center flow was initially overexpanded and then recompressed. This overexpansion and recompresssion is shown in the axial Mach number contours for computational regions 2,3 and 4 of the nozzle in Fig. 14. The contours shown are along the center plane of the nozzle, however, these are similiar to axial plane contours across the nozzle width. The solution for the nozzle exit flow (the fourth axial region at x = 61.81, Fig. 12d) shows velocity vectors indicating fully-developed counter-rotating vorticies with a maximum transverse velocity that is about 10 percent of the axial velocity. The calculated static pressure distribution (Fig. 13d) at the nozzle exit is more uniform than at the other axial stations, and the pressure is highest near the nozzle centerline and lowest in the corners; this is the same trend that was observed experimentally. In Fig. 15 the velocity vectors corresponding to the CFD solution with the isothermal wall assumption are shown for x = 61.81 inches (nozzle exit); these results show the same flow pattern (i.e. fully developed counter rotating vortices along the wall centerline) as did the adiabatic wall solution.

For the AHSTF Mach 6 nozzle and the Mach 4.7 nozzle, some problems were encountered with the turbulence model in the last half of each nozzle. As the vortices developed, the determination of the first maximum in the F-function of the correlation for the outer turbulent viscosity became very difficult. Sudden jumps in calculated turbulent viscosity produced numerical oscillations which resulted in program failure. The calculations were continued by specifying that the maximum value of the F-function occurred at a prescribed distance (number of nodes) from the wall. This assumption allowed the simulation to continue until a solution was obtained; however, it may have affected the resulting calculations in the boundary layer and might also account for some of the discrepancies between the experimental and computational results.

These CFD results are considered preliminary and refined calculations are being continued at NASA Langley. The calculated parameters, however, compare sufficiently well with the experimental data that the nature of the flow development is indicated. The numerical results show that the AHSTF Mach 6 nozzle expansion flow includes sets of counter-rotating vorticies, which is a flow phenomenon that could not be determined from the

experimental results since only axial flow measurements were obtained.

**AHSTF Mach 4.7 Nozzle**

The fourth computed test case involved CFD simulation of the AHSTF Mach 4.7 nozzle flow using a 151 x 60 x 60 grid (over 3 axial regions), turbulence model activated, a subsonic inflow condition with a Mach number of approximately 0.4 and an adiabatic wall assumption. The nozzle geometry analysed included an approximately constant area nozzle extension which was not installed during the nozzle calibration tests (Ref. 1) and was not shown on Fig. 2. Axial flow property contours, however, (axial Mach number contours will be presented later) show no significant changes in the nozzle flow properties through this extension. Therefore, the CFD results at the nozzle exit which were made including the extension were compared to the experimental calibration which were obtained with the extension removed. The resultant contours are shown in Fig. 16. Comparison of the computed contours with the experimental contours of Fig. 6 shows that the computational results again (as in the Mach 6 case) indicate substantially higher flow gradients near the centerline of the walls than did the experimental results. This is further demonstrated by comparison of experimental and calculated centerline profiles of various parameters in Fig. 17. The CFD and experimental results compare well near the center of the nozzle at locations more than two inches from the wall. The flow property gradients within two inches of the wall are greater from the CFD solution than from the experimental results.

Figures 18 and 19 show transverse velocity vectors and static pressure ratio contours at three axial stations down the length of the AHSTF Mach 4.7 nozzle. These figures show a flow development similiar to that discussed previously for the AHSTF Mach 6 nozzle; however, these results indicate that two smaller vorticies exist near the nozzle wall centerline (symmetry plane) where a single vortex was predicted in the Mach 6 case, Fig. 20 shows axial Mach number contours along the center plane of the AHSTF Mach 4.7 nozzle which also indicates a flow which is initially overexpanded and then recompressed since the highest Mach number regions exist near the beginning of region 3 and a lower Mach number is seen at the exit.

**Concluding Remarks**

Complete Navier-Stokes solutions have been obtained for the flow in Mach 4.7 and Mach 6 square cross-section contoured facility nozzles. These nozzles are used in scramjet engine testing in NASA Langley's Arc-Heated Scramjet Test Facility. The numerical results show general, but not complete, agreement with earlier experimental measurements. Parameter contour plots of the numerical and the experimental data at the exits of the nozzles are similar. More detailed comparisons show excellent agreement in the center flow areas of the nozzles; however, agreement is not good within two inches of the wall in the approximately 11 inch x 11 inch nozzle exit areas. Accepting the premise that the numerical calculations could be as accurate as the experimental measurements near the wall, the flow development was traced along the axial length of the nozzle.

The numerical results showed the formation of counter-rotating vortices on the centerline of each sidewall (maximum transverse-to-axial velocity ratio of 0.10 at the nozzle exit). With facility nozzle boundary layer ingestion into scramjet engines, one set of these vortices would enter the engine. Without boundary layer ingestion, the entering flow would be relatively uniform and vortex free.

**TABLE 1**

| | AHSTF Mach 6 Nozzle | AHSTF Mach 4.7 Nozzle |
|---|---|---|
| $P_{t,1}$(psia) | 584 | 177 |
| $T_{t,1}$(°R) | 3,965 | 2,641 |
| MW | 28.964 | 28.964 |
| Cp/Cv | 1.4 | 1.4 |

**References**


1. Thomas, Scott R.; Voland, Randall T.; and Guy, Robert W.: Test Flow Calibration Study of the Langley Arc-Heated Scramjet Test Facility. AIAA/SAE/ASME/ASEE 23rd Joint Propulsion Conference, AIAA Paper 87-2165, June 29-July 2, 1987.

2. Kumar, Ajay: Numerical Simulation of Scramjet Inlet Flowfields. NASA TP-2517, May 1986.

3. Kumar, Ajay: User's Guide for NASCRIN-A Vectorized Code for Calculating Two-Dimensional Supersonic Internal Flow Fields. NASA TM-85708, February 1984.

4. MacCormack, R. W.: A Numerical Method for Solving the Equations of Compressible Viscours Flow. AIAA-81-0110, January 1981.

5. Baldwin, Barrett and Lomax, Harvard: Thin-Layer Approximation and Algebraic Model for Separated Turbulent Flows. AIAA Paper 78-257, January 1978.

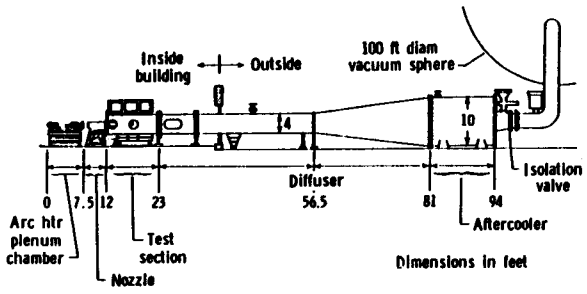


Figure 1.- Elevation view of the Arc-Heated Scramjet Test Facility (AHSTF).

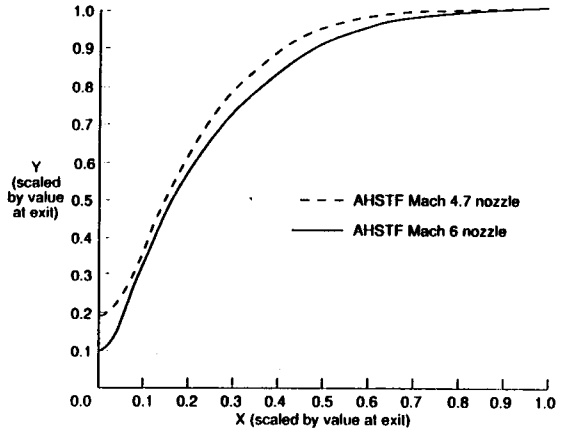


Figure 4.- Nozzle wall contours.

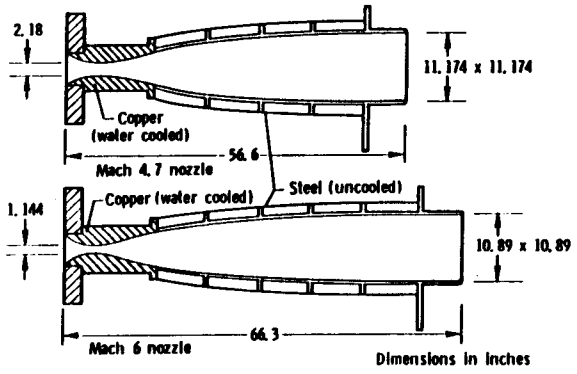


Figure 2.- Arc-Heated Scramjet Test Facility Nozzle Schematics.

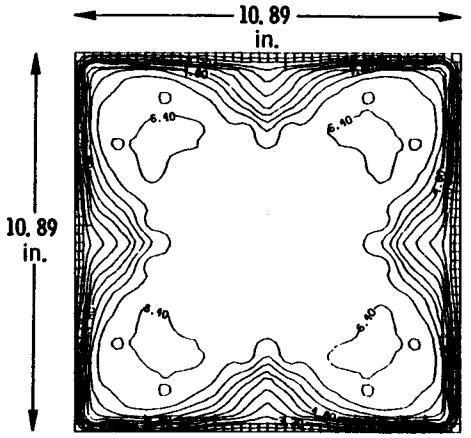


a.- Mach number ($M_1$)

Figure 5.- Experimental contours of flow parameters at the exit of the Mach 6 nozzle.

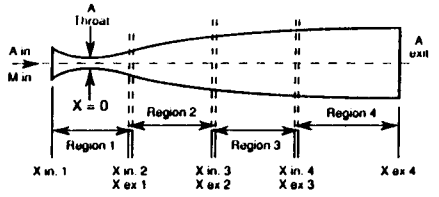


| Test case | Nozzle simulated | A in. | A Throat | A exit | Region 1 Grid size (X) x (Y) x (Z) | Region 2 Grid size (X) x (Y) x (Z) | Region 3 Grid size (X) x (Y) x (Z) | Region 4 Grid size (X) x (Y) x (Z) |
|---|---|---|---|---|---|---|---|---|
| | Turbulence model | M in | | | X in. 1 / X ex 1 | X in. 2 / X ex 2 | X in. 3 / X ex 3 | X in. 4 / X ex 4 |
| 1 | AHSTF Mach 6 | 1.309 | 1.309 | 118.6 | 30 x 50 x 50 | 24 x 50 x 50 | 35 x 50 x 50 | 35 x 50 x 50 |
| | Laminar | 1.01 | | | 0 / 4 | 3.809 / 9.5 | 9.187 / 25 | 24.342 / 61.811 |
| 2 | AHSTF Mach 6 | 1.309 | 1.309 | 118.6 | 45 x 75 x 75 | 43 x 75 x 75 | 48 x 75 x 75 | 48 x 75 x 75 |
| | Laminar | 1.01 | | | 0 / 4 | 3.78 / 10 | 9.61 / 25 | 23.978 / 61.811 |
| 3 | AHSTF Mach 6 | 1.309 | 1.309 | 118.6 | 45 x 75 x 75 | 43 x 75 x 75 | 48 x 75 x 75 | 48 x 75 x 75 |
| | Turbulent | 1.01 | | | 0 / 4 | 3.78 / 10 | 9.61 / 25 | 23.978 / 61.811 |
| 4 | AHSTF Mach 4.7 | 7.62 | 4.75 | 124.9 | 46 x 60 x 60 | 47 x 60 x 60 | 62 x 60 x 60 | N/A |
| | Turbulent | 40 | | | -1.943 / 6 | 5.785 / 20 | 19.571 / 67.092 | N/A / N/A |

Dimensions in inches or $in.^2$

Figure 3.- Geometry and Grid Size used in CFD calculations.

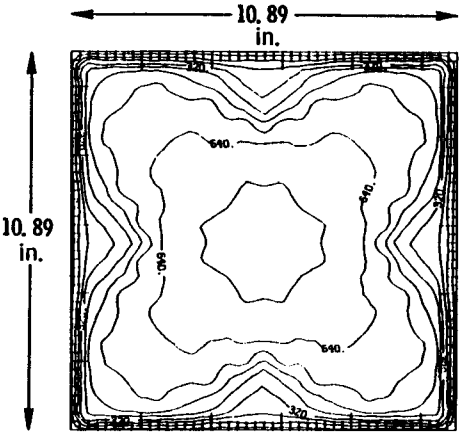


b.- Mass Flow Rate per Unit Area ($lbm/s\text{-}in.^2 \times 10^4$).

Figure 5.- Continued.

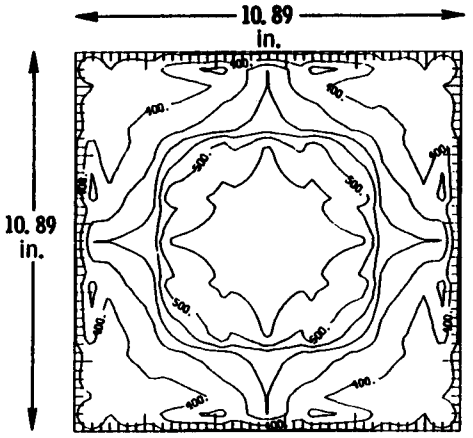


c.- Static-to-total pressure ratio ($P_1/P_{t,1} \times 10^6$).

Figure 5.- Concluded.

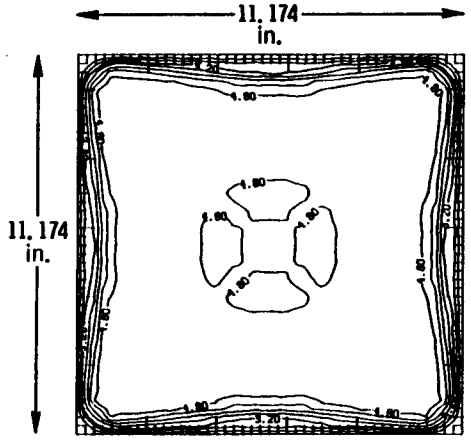


a.- Mach number ($M_1$)

Figure 6.- Experimental contours of flow parameters at the exit of the Mach 4.7 nozzle.

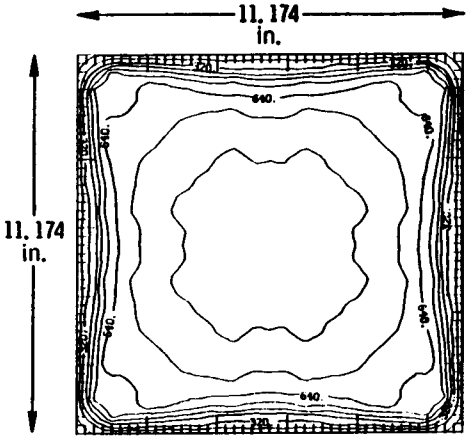


b.- Mass Flow Rate per Unit Area ($lbm/s\text{-}in^2 \times 10^4$).

Figure 6.- Continued.

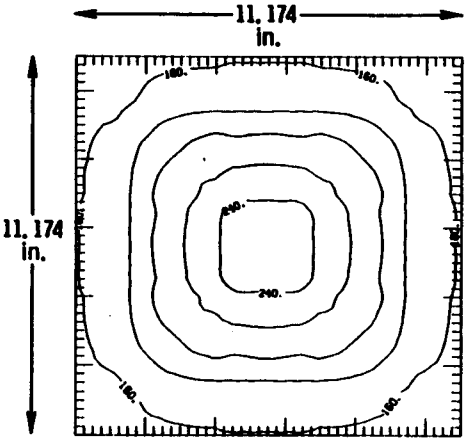


c.- Static-to-total pressure ratio ($P_1/P_{t,1} \times 10^5$).

Figure 6.- Concluded.

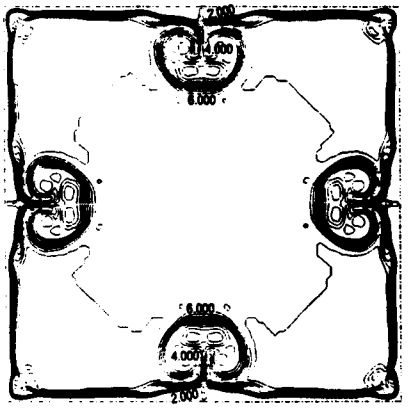

Figure 7.- Calculated contour plot of Mach number at the exit of the Mach 6 nozzle from moderate grid laminar solution (adiabatic wall boundary condition).

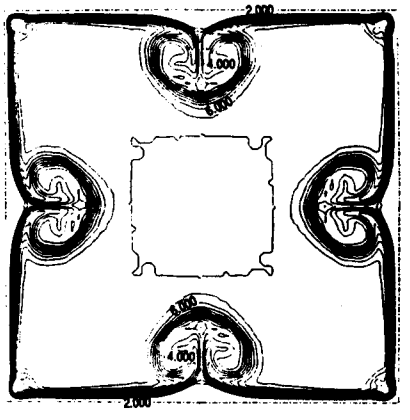

Figure 8.- Calculated contour plot of Mach number at the exit of the Mach 6 nozzle from fine grid laminar solution (adiabatic wall boundary condition).

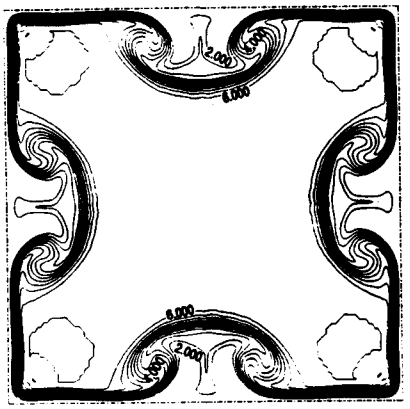


a.- Mach number

Figure 9.- Calculated flow parameter contours at the exit of the Mach 6 nozzle. (Turbulent flow, adiabatic wall boundary condition.)

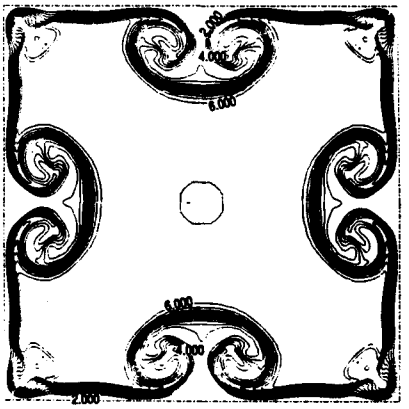


a.- Mach number.

Figure 10.- Calculated flow parameter contours at the exit of the Mach 6 nozzle. (Turbulent flow, isothermal wall boundary condition [1000°R].)

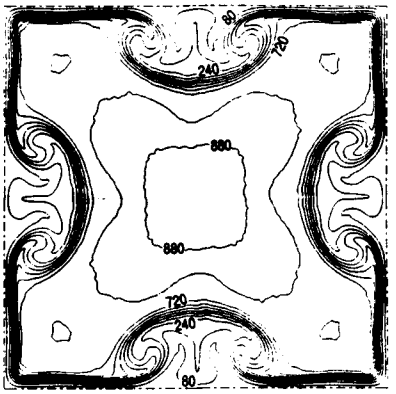


b.- Mass Flow Rate per Unit Area ($lbm/s\text{-}in^2 \times 10^4$).

Figure 9.- Continued.

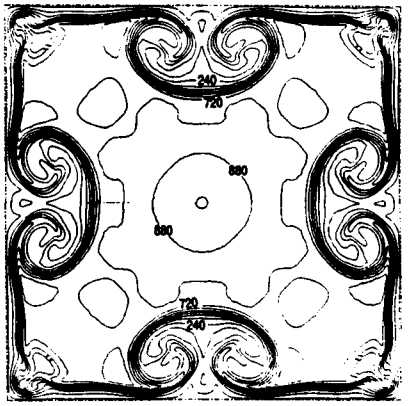


b.- Mass Flow Rate per Unit Area ($lbm/s\text{-}in^2 \times 10^4$).

Figure 10.- Continued.

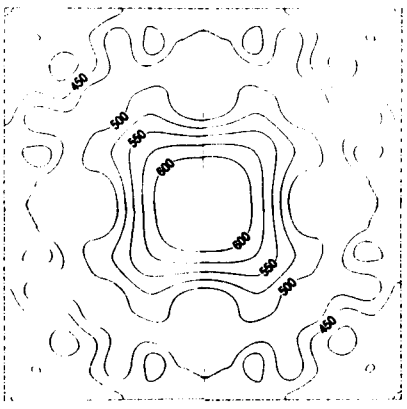


c.- Static-to-total pressure ratio ($P_1/P_{t,1} \times 10^6$).

Figure 9.- Concluded.

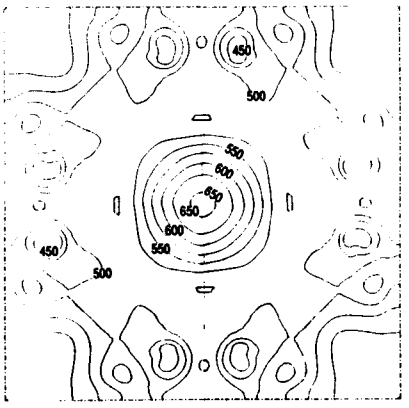


c.- Static-to-total pressure ratio ($P_1/P_{t,1} \times 10^6$).

Figure 10.- Concluded.

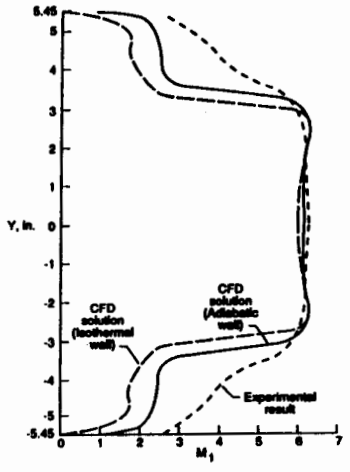


a.- Mach number.

Figure 11.- Comparison of calculated and experimental flow parameter profiles on the exit centerline of the Mach 6 nozzle.

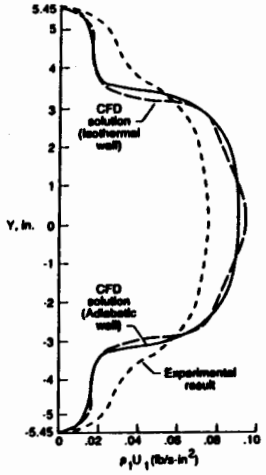


b.- Mass Flow Rate per Unit Area.

Figure 11.- Continued.

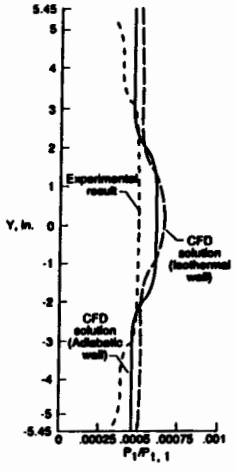


c.- Static-to-total pressure ratio.

Figure 11.- Continued.

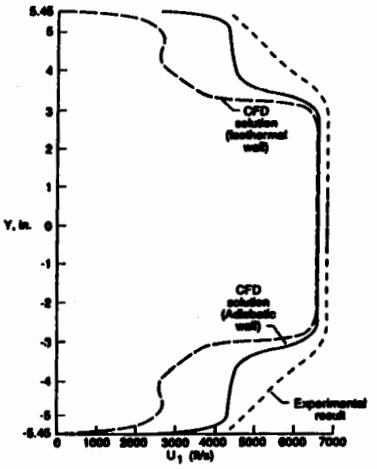


d.- Velocity

Figure 11.- Continued.

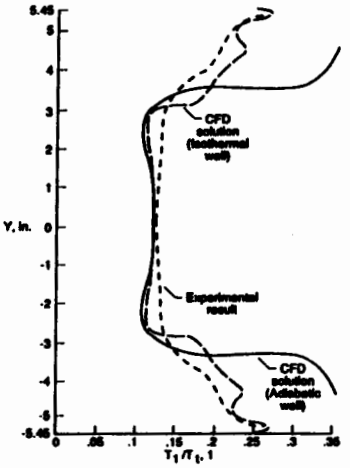


e.- Static-to-total temperature ratio

Figure 11.- Concluded.

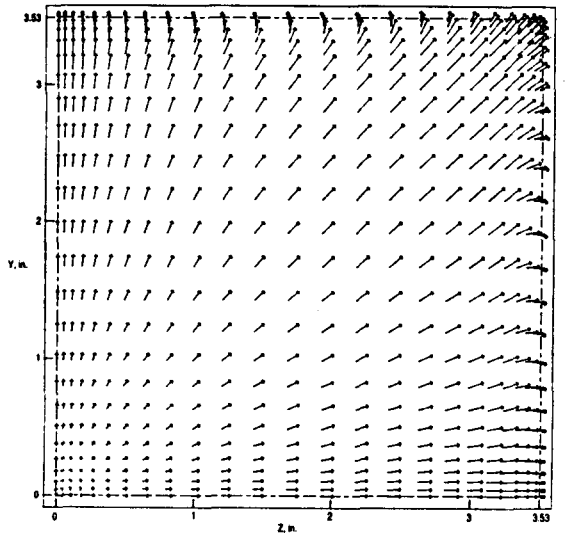

a.- x = 14.93 inches

Figure 12.- Calculated velocity vectors in transverse planes along the length of the Mach 6 nozzle (adiabatic wall, one quadrant shown).

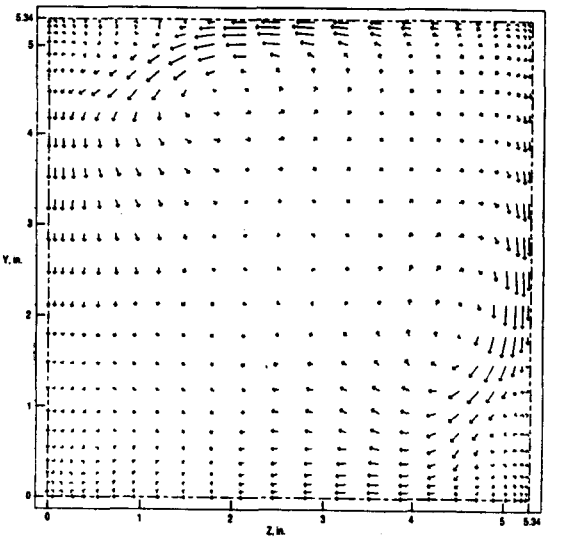

c.- x = 45.10 inches

Figure 12.- Continued.

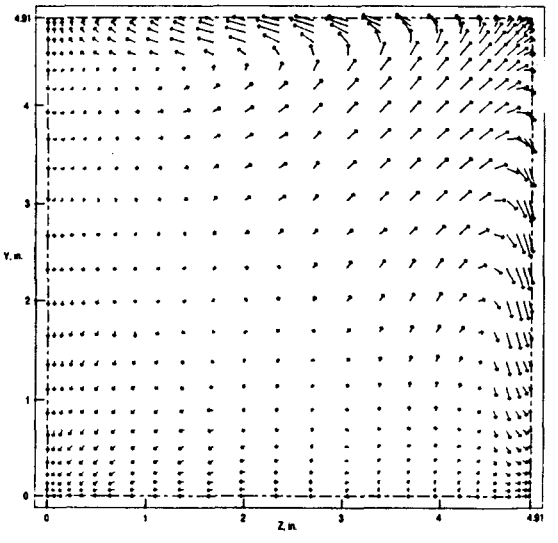

b.- x = 30.12 inches

Figure 12.- Continued.

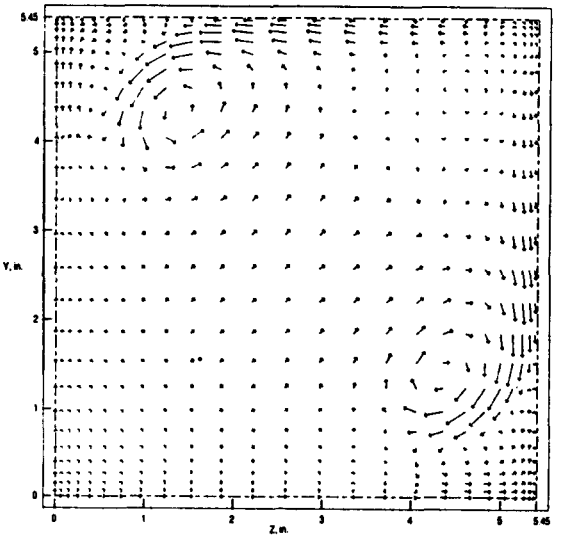

d.- x = 61.81 inches (nozzle exit)

Figure 12.- Concluded.

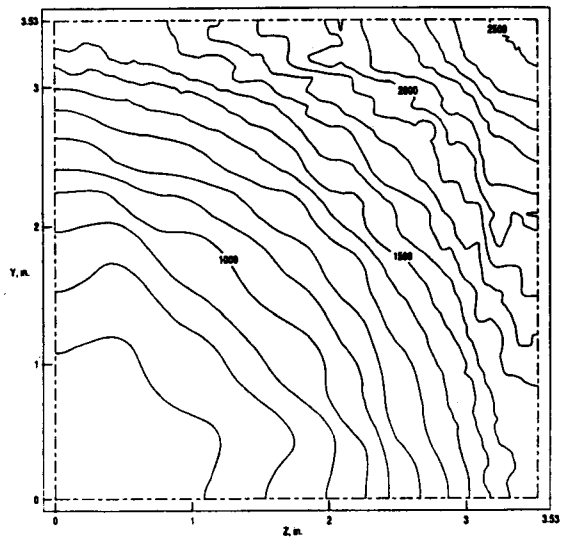

a.- x = 14.93 inches

Figure 13.- Calculated static-to-total pressure ratio contours in transverse planes along the length of the Mach 6 nozzle (adiabatic wall, one quadrant shown) ($P_1/P_{t,1}$ x $10^6$).

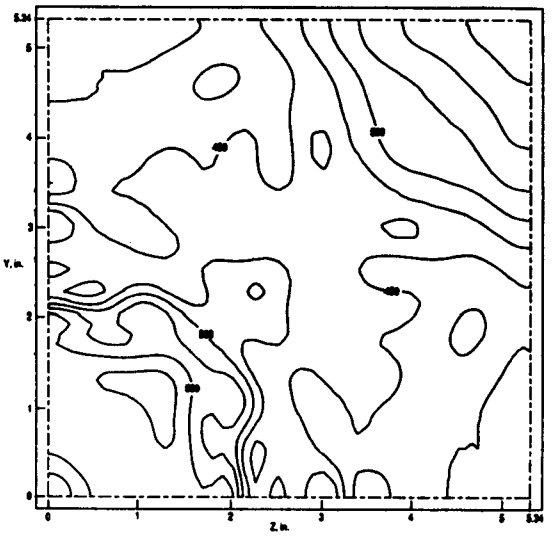

c.- x = 45.10 inches

Figure 13.- Continued.

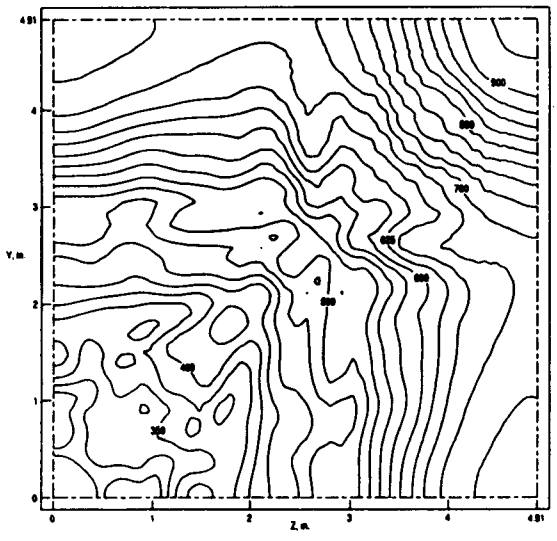

b.- x = 30.12 inches

Figure 13.- Continued.

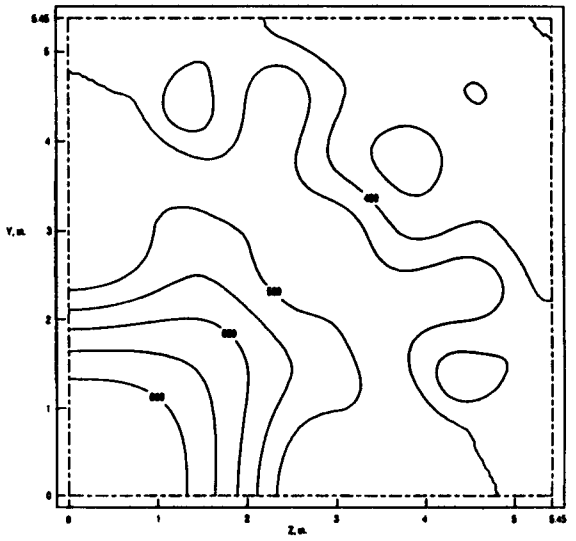

d.- x = 61.81 inches (nozzle exit)

Figure 13.- Concluded.

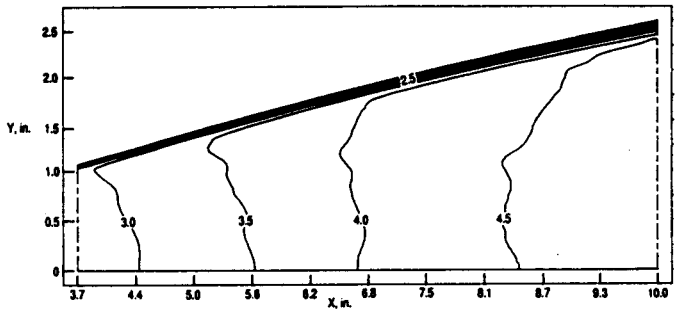


a.- Computational Region 2.

Figure 14.- Calculated axial Mach number contours along the center plane of the Mach 6 nozzle.

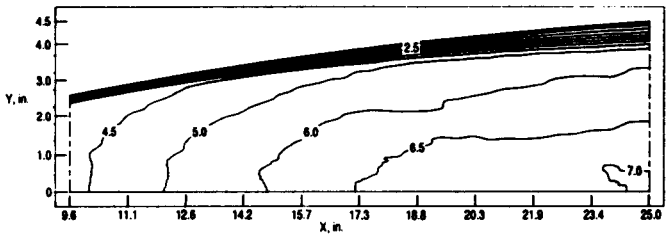


b.- Computational Region 3.

Figure 14.- Continued.

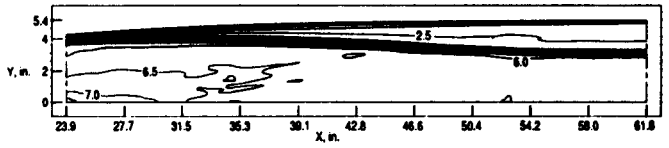


c.- Computational Region 4.

Figure 14.- Concluded.

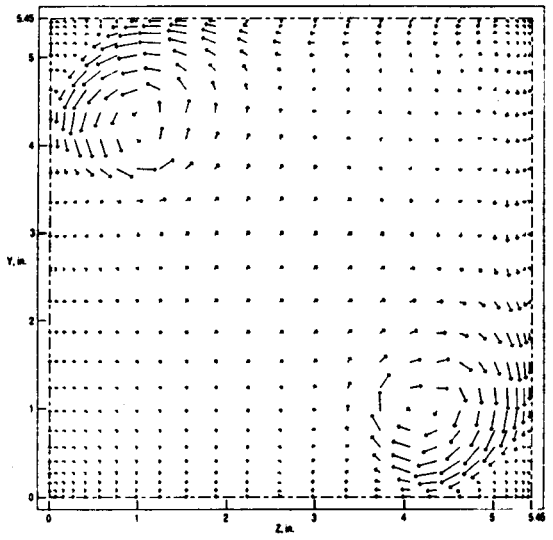


Figure 15.- Calculated velocity vectors in the transverse plane at the exit of the Mach 6 nozzle (Isothermal wall [1000°R]).

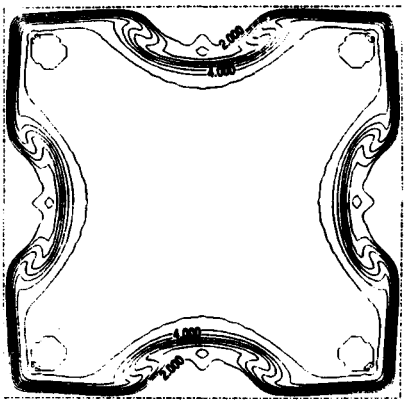

a.- Mach number.

Figure 16.- Calculated flow parameter contours at the exit of the Mach 4.7 nozzle (turbulent flow, adiabatic wall boundary condition).

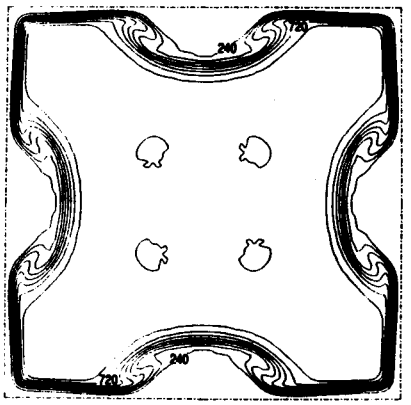


b.- Mass Flow Rate per Unit Area ($1bm/s-in^2 \times 10^4$).

Figure 16.- Continued.

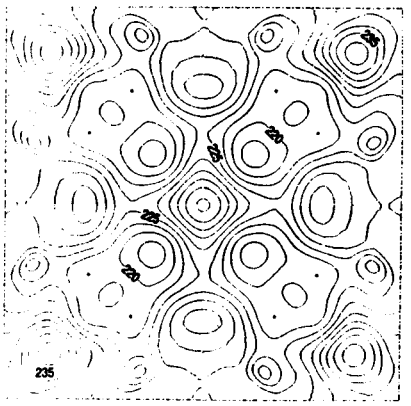


c.- Static-to-total pressure ratio ($P_1/P_{t,1} \times 10^5$)

Figure 16.- Concluded.

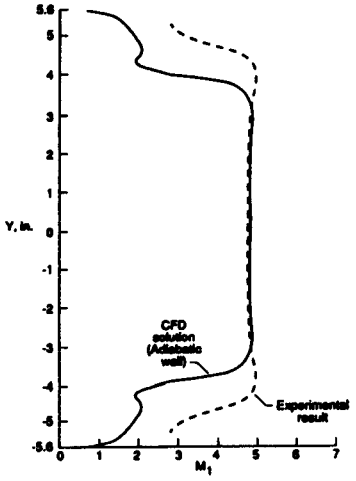


a.- Mach number

Figure 17.- Comparison of calculated and experimental flow parameter profiles on the exit centerline of the Mach 4.7 nozzle.

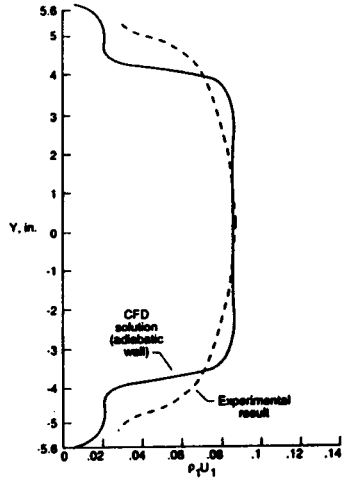


b.- Mass Flow Rate per Unit Area (lbm/s-in$^2$)

Figure 17.- Continued.

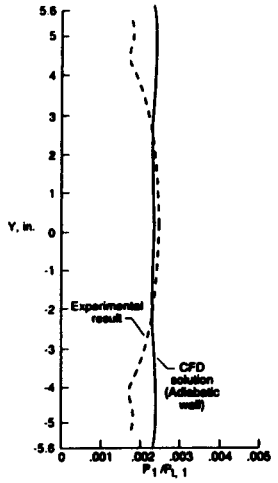


c.- Static-to-total pressure ratio.

Figure 17.- Continued.

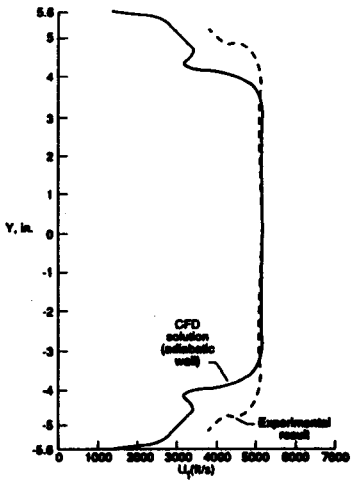


d.- Velocity

Figure 17.- Continued.

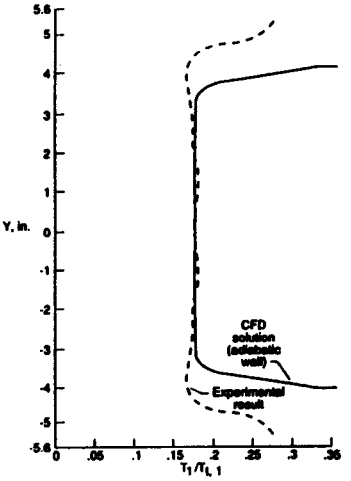


e.- Static-to-total temperature ratio.

Figure 17.- Concluded.

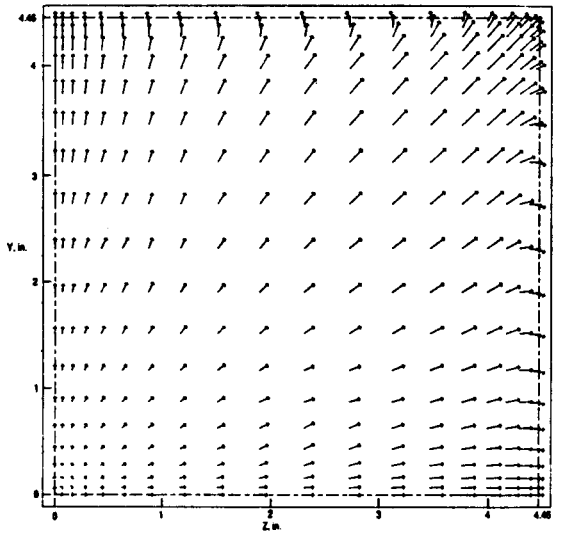

a.- x = 20.44 inches

Figure 18.- Calculated velocity vectors in transverse planes along the length of the Mach 4.7 nozzle (adiabatic wall, one quadrant shown).

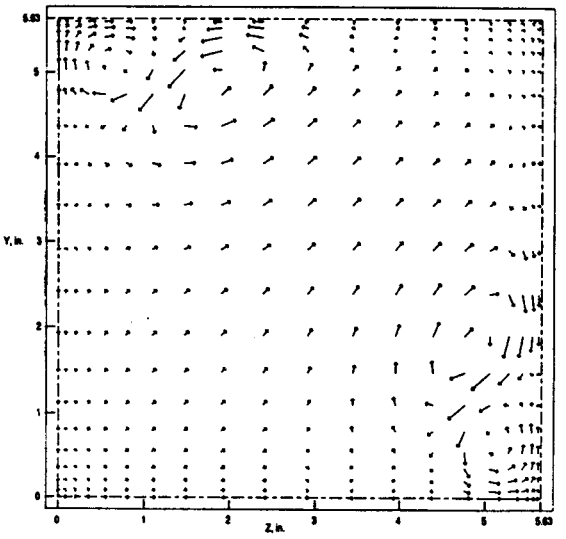

c.- x = 67.09 inches (nozzle exit).

Figure 18.- Concluded.

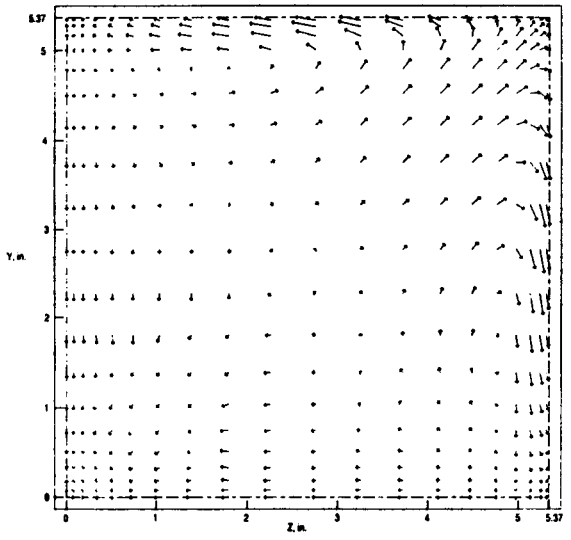

b.- x = 34.37 inches

Figure 18.- Continued.

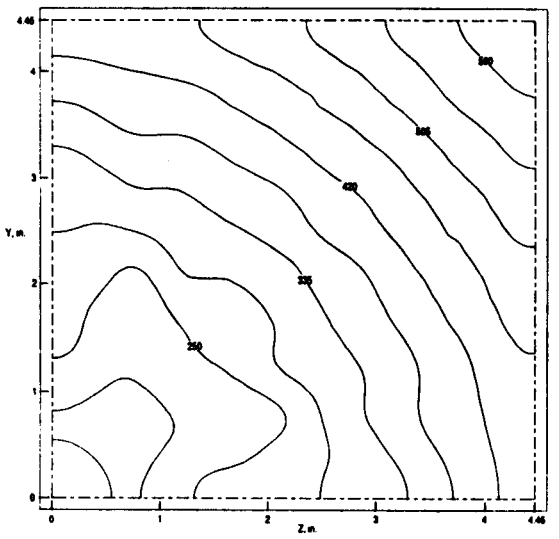

a.- x = 20.44 inches

Figure 19.- Calculated static-to-total pressure ratio contours in transverse planes along the length of the Mach 4.7 nozzle (adiabatic wall, one quadrant shown) ($P_1/P_{t,1} \times 10^5$).

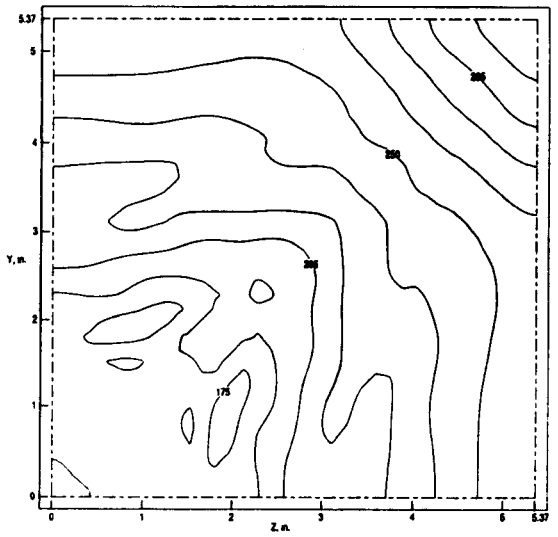


b.- x = 34.37 inches

Figure 19.- Continued.

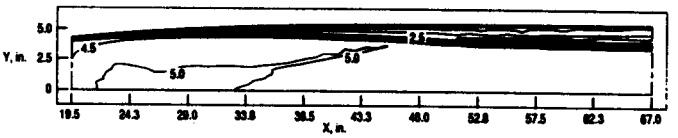


Figure 20.- Calculated axial Mach number contours along the center plane of the Mach 4.7 nozzle for computational region 3.

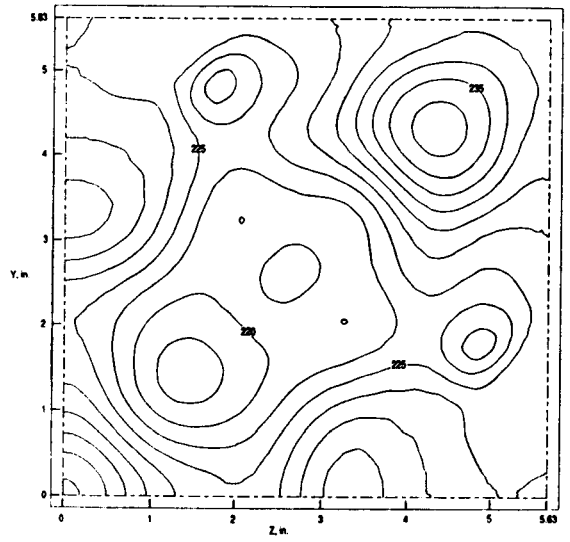


c.- x = 67.09 inches (nozzle exit).

Figure 19.- Concluded.